ORIGINAL ARTICLE

WILEY

SARS-CoV-2 infection aggravates chronic comorbidities of cardiovascular diseases and diabetes in mice

Yuanwu Ma[1,2] iD | Dan Lu[1,2] | Linlin Bao[1,2] | Yajin Qu[1,2] | Jiangning Liu[1,2] | Xiaolong Qi[1,2] | Lei Yu[1,2] | Xu Zhang[1,2] | Feifei Qi[1,2] | Qi Lv[1,2] iD | Yunpeng Liu[1,2] | Xudong Shi[1,2] | Caixian Sun[1,2] | Jing Li[1,2] | Jie Wang[1,2] | Yunlin Han[1,2] | Kai Gao[1,2] | Wei Dong[1,2] | Ning Liu[1,2] | Shan Gao[1,2] | Jing Xue[1,2] iD | Qiang Wei[1,2] | Sidan Pan[1,2] | Hong Gao[1,2] | Lianfeng Zhang[1,2] iD | Chuan Qin[1,2] iD

[1]Key Laboratory of Human Disease Comparative Medicine, National Health Commission of China (NHC), Institute of Laboratory Animal Science, Peking Union Medicine College, Chinese Academy of Medical Sciences, Beijing, China

[2]Beijing Engineering Research Center for Experimental Animal Models of Human Critical Diseases, Institute of Laboratory Animal Science, Peking Union Medicine College, Chinese Academy of Medical Sciences, Beijing, China

Correspondence
Chuan Qin, #5 Panjiayuan Nanli, Chaoyang District, Beijing, China.
Email: qinchuan@pumc.edu.cn

Abstract

Background: Cardiovascular diseases (CVDs) and diabetes mellitus (DM) are top two chronic comorbidities that increase the severity and mortality of COVID-19. However, how SARS-CoV-2 alters the progression of chronic diseases remain unclear.

Methods: We used adenovirus to deliver h-ACE2 to lung to enable SARS-CoV-2 infection in mice. SARS-CoV-2's impacts on pathogenesis of chronic diseases were studied through histopathological, virologic and molecular biology analysis.

Results: Pre-existing CVDs resulted in viral invasion, ROS elevation and activation of apoptosis pathways contribute myocardial injury during SARS-CoV-2 infection. Viral infection increased fasting blood glucose and reduced insulin response in DM model. Bone mineral density decreased shortly after infection, which associated with impaired PI3K/AKT/mTOR signaling.

Conclusion: We established mouse models mimicked the complex pathological symptoms of COVID-19 patients with chronic diseases. Pre-existing diseases could impair the inflammatory responses to SARS-CoV-2 infection, which further aggravated the pre-existing diseases. This work provided valuable information to better understand the interplay between the primary diseases and SARS-CoV-2 infection.

KEYWORDS
Cardiovascular disease, COVID-19, diabetes mellitus, mouse model, SARS-CoV-2

1 | INTRODUCTION

Severe acute respiratory syndrome coronavirus 2 (SARS-CoV-2) causes coronavirus disease 2019 (COVID-19) in human and has become a worldwide pandemic. COVID-19 is more severe and lethal in patients with other chronic diseases. Cardiovascular diseases (CVDs) and diabetes mellitus (DM) are the top two comorbidities that aggravate COVID-19.[1-4] In one meta-analysis of 44, 672

COVID-19 patients, CVDs and DM are associated with 22.7% and 19.7% mortality rates, respectively. These numbers are higher than the mortality without comorbidities.[2] A similar observation was also reported in severe acute respiratory syndrome (SARS) epidemic in 2002/2003.[5] Therefore, understanding the mutual influences between comorbidities and COVID-19 is critical for the development of better strategies to control and treat these diseases.

Human angiotensin-converting enzyme 2 (hACE2) is the receptor of SARS-CoV-2 that interacts with the spike (S) protein and mediates viral entry into the cells.[6] Although the murine ortholog of ACE2 (mACE2) presents over 81% similarity with hACE2, mACE2 is not capable to mediate SARS-CoV-2 infection. Therefore, ectopic expression of hACE2 is necessary for SARS-CoV-2 to infect murine cells.[6-9] Several hACE2 transgenic mice has been developed to study the infection mechanisms and pathogenicity of SARS-CoV-2.[7-9] Although these mice can be bred with other murine disease models to investigate the interactions between comorbidities and COVID-19, this strategy is slow and expensive. Alternatively, several groups recently established adenovirus-based hACE2 delivery systems to murine lungs, and built a quick and convenient approach to sensitize the mice for SARS-CoV-2 infection and COVID-19 pathogenesis.[10,11]

Here we optimized a virus-based approach to deliver hACE2 to murine models of CVDs and DM, and investigated the mutual impacts between these preexisting diseases and SARS-CoV-2 infection. We found that preexisting CVDs and DM aggravated the pathological phenotypes of pneumonia and impairment of the immune response due to SARS-CoV-2 infection. Underlying CVDs increased the risk of SARS-CoV-2 virus particle invasion in myocardium. SARS-CoV-2 infection aggravated myocardial defeats in CVD models, and accumulated oxidative stress and activated apoptosis pathway induced by inflammation contribute to myocardial injury. In diabetic mice, SARS-CoV-2 infection resulted in increased blood glucose and abnormal glucose tolerance, and significantly decreased bone mineral density (BMD). Taken together, our comorbid mouse models mimicked the complex pathological symptoms of COVID-19 patients with preexisting cardiovascular disease or diabetes. They both showed impairments of immune response during SARS-CoV-2 infection, which result in damage to disease-related target organs. Our results provided valuable information for better understanding of mutual impacts between these preexisting chronic diseases and COVID-19.

2 | METHODS

2.1 | Animals and ethics statement

Specific pathogen-free, 6- to 10-week male C57BL/6, BABL/c, and ob/ob mice were purchased from Beijing HFK BIOSCIENCE CO., LTD. cTnT^R141W transgene mice was preserved at Institute of Laboratory Animal Science, Peking Union Medicine College, Chinese Academy of Medical Sciences. Experiments were performed in an Animal Biosafety Level 3 (ABSL3) facility using HEPA-filtered isolators. All animal experiments were approved by the Institutional Animal Care and Use Committee of the Institute of Laboratory Animal Science, Peking Union Medical College (MYW20009). All the experiments complied with all relevant ethical regulations.

2.2 | Ad5-hACE2 transduction in mice

Mice were anesthetized with isoflurane and intranasally administered with 2.5×10^8 Ad5-hACE2 or Ad5-Empty in 50 μL DMEM. To detect hACE2 expression after Ad5-hACE2 transduction, C57BL/6 mice lungs were collected at day 0, 3, 5, 7, 10, 15, 20, and 30. The human ACE2 expression was detected using western blot and real-time PCR.

2.3 | SARS-CoV2 infection of Ad5-hACE2–transduced mice

Five to seven days post–Ad5-hACE transduction, mice were intranasally infected with SARS-CoV-2 stock virus at a dosage of 10^5 TCID$_{50}$ or PBS as mock infection control. The viral copies in mice lung or other tissues were using the methods described before.[7,12,17] Mice were observed and weighted daily. All animal infection experiment was performed in Biosafety Level 3 (BSL3) Laboratories of Institute of Laboratory Animal Science, Peking Union Medicine College, Chinese Academy of Medical Sciences.

2.4 | RNA extraction and real-time PCR

Total RNA was isolated from tissues using TRIzol Reagent (15596018, Thermo Fisher). The cDNA was synthesized using total RNA follow the instruction of Superscript III reverse transcriptase manufacturer's protocol (RR047A, TaKaRa). Primers used for real-time PCR detection are listed in Table S1.

2.5 | Total protein extraction and western blot

Total protein lysates of different tissues were obtain as described before.[22] We use SDS-PAGE to separate the protein and use target antibody to detect the express in nitrocellulose membranes. Antibody including anti human ACE2 antibody (1:250 dilution, MAB933, R&D) and cTnI antibody (1:1000 dilution, ab47003, Abcam).

2.6 | Histology and immunohistochemisty

Major organs were grossly examined in the ABSL3 laboratory and then fixed in 10% buffered formalin solution and then paraffin sections (3-4 μm) were prepared. Hematoxylin and eosin (H&E) staining and modified Masson's Trichrome staining were performed to

determine the histopathologic changes as described before.[7,12,17] Paraffin sections of lungs or hearts were used for the expressional distribution of several proteins. Briefly, sections were dewaxed and rehydrated, and heat-induced antigen retrieval routinely. Then the sections were blocked and incubated with appropriate primary and secondary antibodies. Antibody to hACE2 (1:50 dilution, MAB933, R&D Systems), rabbit polyclonal antibody to SARS-Cov-2 Spike antibody (1:100 dilution, 21804, SIgnalway), CD4 (1:1000 dilution, ab183685, Abcam), CD8 (1:2000 dilution, ab217344, Abcam), and Mac (1:1000 dilution, Cl8942AP, Cedarlane) were used as the primary antibody. For immunohistochemical analysis, a secondary kit (Beijing ZSGB Biotechnology) were used, followed determination using an Olympus microscope. For immunofluorescence analysis of SARS-CoV-2 antigen, a secondary antibody conjugated with FITC (goat anti-rabbit, A11008, Invitrogen) and TRITC (goat anti-mouse, A21424, Invitrogen) were used, followed by fluorescence microscopy. For hexamine silver staining, briefly, sections of hearts were in turn treated with periodic acid, hexamine silver, gold chloride, and sodium thiosulfate, and finally stained with nuclear solid red, followed determination via a Olympus microscope.

2.7 | In situ hybridization (ISH)

Major organs were grossly examined in the ABSL3 laboratory, fixed in 10% buffered formalin solution, and then paraffin sections (3-4 μm) were prepared. The virus infection was detected using a RNAscope 2.5 HD reagent kit (322300, Advanced cell diagnostics). Briefly, sections were routinely dewaxed and treated with H_2O_2 and protease reagents (REF:322330; LOT:2009712). Probe were incubated at 40℃(REF:848561; LOT:20233D) and detected with DAB reagent (REF:322310; LOT:2008935). Finally, sections were stained with hematoxylin, followed determination via microscopy.

2.8 | ELISA

The N-Terminal Pro Brain Natriuretic Peptide (NT-proBNP) in peripheral blood was determined using an enzyme-linked immunosorbent assay (ELISA) kit (orb441265, Biorbyt). Briefly, 96-well plates in the kit were precoated with the target antibody; the tested serum was diluted with the diluent provided in the kit (1:5), added into the appropriate wells, and then incubated for 2 hours at 37℃. After the incubation with the secondary antibody for 1 hr at 37℃, plates were washed five times with wash solution. The reaction was developed by TMB substrate reagent and then stopped after 15 minutes by adding the stop solution provided by the kit. Plates were then read at a wavelength of 450 nm.

2.9 | Fasting and fasted blood glucose

For blood glucose and biochemistry analysis, the ob/ob mice were deprived from food except free accesses to water for 16 hours (21:00 PM to 9:00 AM). The fasted blood glucose was measured from tail blood by an ONETOUCH UltraEasy glucometer (Johnson, US).

2.10 | Insulin sensitivity evaluation

Insulin tolerance test (ITT) was performed as previously described.[35] Briefly, ob/ob mice were fasted for 4 hours (9:00 AM-13:00 PM). Blood samples were collected from tail for determination of baseline values of blood glucose ($t = 0$). The mice were then intraperitoneal injected with human insulin 1 U/kg, and then blood glucose was measured at 15, 30, 60, 90, and 120 minutes after insulin injection. The values of area under the glucose-time curve (AUC) were calculated.

2.11 | Serum biochemistry

For serum biochemistry, the fasted serum was collected from vein after the measurement of fasted blood glucose. The levels of TG, TC, LDL, HDL, r-GT, ALP, AST, and ALT were measured using a TBA2000FR biochemical analyzer (TOSHIBA, Japan).

2.12 | Microcomputed tomography (micro-CT) analysis

The mice lower limbs (femur and tibia) were dissected and collected for the micro-CT measurements. The femurs of the mice were scanned using micro-CT (Siemens Inveon, Germany) with resolution of 10.3 μm at tube voltage of 60 kV and current of 400 μA. Two millimeter below the center of the epiphyseal line with 100 slices was selected as the region of interest (ROI) for the analysis. The micro-architectural parameters: bone mineral density (BMD, mg/cm³), relative bone volume (BV/TV), trabecular number (Tb.N), trabecular thickness (Tb.Th), and trabecular separation (Tb.Sp) were measured using Inveon Research Workplace III software (Germany).

2.13 | Statistical analysis and software

All data were analyzed with GraphPad Prism 8.0 software. Comparisons between two groups were made by unpaired two-tailed Student's t tests. All values are expressed as mean ± s.e.m. $*P < .05$, $**P < .01$, $***P < .001$ for two-tailed Student's t tests, unless stated otherwise.

3 | RESULTS

3.1 | Generation of a rapid and flexible method for comorbid mice model with SARS-CoV-2 infection

To establish a robust hACE2 delivery system targeting murine lungs, we first intranasally treated 6- to 10-week-old C57BL/6 mice with

three different viral vectors and compared their efficiency in gene delivery. The dosages and vectors included 2.5×10^8 TU lentivirus (lenti-hACE2), 2.5×10^8 PFU replication-deficient adenovirus (Ad5-hACE2), and 1.0×10^{12} vg/mL adeno-associated virus (AAV6-hACE2). At 0, 3, 5, 7, and 10 days after transduction (d.a.t.), we performed real-time PCR to measure hACE2 expression in murine lungs. We found adenoviral vectors established faster and higher hACE2 expression as compared to the other methods. (Figure S1A,B).

Next, we focused on the Ad5-hACE2 approach and explored the dynamics of exogenous hACE2 expression. We determined hACE2 expression in the lungs at 3, 5, 7, 10, 15, 20, and 30 d.a.t. by real-time PCR and western blot (Figure S1C-E, n = 3 at each time point). Two ACE2 antibodies were used in western blot, one recognizing both mACE2 and hACE2 (Figure S1D), and the other specifically probing hACE2 (Figure S1E). This experiment showed the ectopic hACE2 expression peaked between 5 and 7 d.a.t.

We further increased the dose of Ad5-hACE2 and re-administered the virus to the same animals. However, these experiments did not further enhance hACE2 expression levels (Figure S1F,G). The immunohistochemistry analysis showed that hACE2 was predominantly expressed in the alveolar epithelium (Figure S1H). After optimization of the hACE2 transduction strategy, we successfully infected wild-type (WT) C57BL/6 mice with 10^5 TICD$_{50}$ of SARS-CoV-2 or mock virus (Figure S1I). Together, we have established the approach that permits SARS-CoV-2 research in disease mouse models.

3.2 | Preexisting CVDs and DM exacerbates aggravated histopathologic changes of pneumonia during SARS-CoV-2 infection

We used two CVD and one DM mouse models to study the impacts of preexisting disease on SARS-CoV-2 infection and pneumonia-related phenotypes.

In the first CVD model, we treated mice with adriamycin (ADR), a well-established chemical that induced stress and injury in the myocardium.[12-14] Before Ad5-hACE2 transduction, all ADR administered mice displayed typical cardiac damages that were characterized by enlarged cardiac chambers, reduced ventricular wall thickness, and significantly decreased cardiac functions as detected by echocardiography[12-15] (Figure S2A-G). The ADR-treated mice were first inoculated intranasally with Ad5-hACE2 at day 14 after cessation of ADR treatment and then infected with SARS-CoV-2 (day 19) five days after Ad5-hACE2 inoculation (Figure 1A). The second CVD model in this study was cTnT^{R141W} transgenic mice, which displayed typical familial dilated cardiomyopathy (FDCM) phenotypes including dilated chambers, thin walls, and cardiac dysfunction, and previous reported in our laboratory[12-17] (Figure S3A-G). The cTnT^{R141W} mice were inoculated intranasally first with Ad5-hACE2 at day 0 and then infected with SARS-CoV-2 or mock virus 5 days later (Figure 1B).

The ob/ob mice are well-established mice model that exhibit hyperphagia, a diabetes-like syndrome of hyperglycemia. Here we used the ob/ob mice as diabetes mice model for comorbidities associated with SARS-CoV-2 infection. The ob/ob mice were inoculated intranasally with Ad5-hACE2 at day 0 and then infected with SARS-CoV-2 or mock virus at day 5. All mice were killed for phenotype analysis including virologic, pathological, and molecular biology observations at day 5 (5 dpi) (Figure 1B).

In both CVD models, SARS-CoV-2 infection resulted in weight loss compared with their mock control group. ADR-SARS-CoV-2 mice showed fast weight changes in the first 2 days and temporary weight changes back at day 3, then decrease continued till day 5 (Figure 1C, n = 5 in ADR-mock group and n = 10 in ADR-SARS-CoV-2 group). In the cTnT^{R141W}-SARS-CoV-2 group, body weight changes were also observed, and the weight reached bottom at 5 days post infection (dpi) (Figure 1C, n = 3 in cTnT^{R141W}-mock group and n = 5 in cTnT^{R141W}-SARS-CoV-2 group). During SARS-CoV-2 infection, the ADR-SARS-CoV-2 mice demonstrated reduced activity and slightly bristled furs, but no arched back or decreased response to external stimuli was observed. Other groups appear normal, with no observed phenotypes. Body weight changes between the ob/ob-SARS-CoV-2 and ob/ob-mock groups were more obvious when compared to changes between the WT-SARS-CoV-2 and WT-mock groups (Figure 1D). Furthermore, ob/ob mice showed decreased food intake after SARS-CoV-2 infection (Figure S4A). Symptoms such as arched back and decreased responses to external stimuli were not found after SARS-CoV-2 infection in all groups.

All the mice were killed 5 days after SARS-CoV-2 infection for further pathological and virologic analysis. We observed increased lung weight changes in WT mice with SARS-CoV-2 infection. These changes were more significant in both CVD mouse models with SARS-CoV-2 infection (Figure S4B, P = .0002, ADR-SARS-CoV-2 vs WT-SARS-CoV-2 group; P = .0038, cTnT^{R141W}-SARS-CoV-2 vs WT-SARS-CoV-2 group; n = 4 in WT-mock and WT-SARS-CoV-2 groups; n = 5 in ADR-mock group, n = 10 in ADR-SARS-CoV-2 group; n = 3 in cTnT^{R141W}-mock group, n = 5 in cTnT^{R141W}-SARS-CoV-2 group). Lung weight changes between the ob/ob-SARS-CoV-2 and ob/ob-mock groups were more significant when compared with the changes between the WT-SARS-CoV-2 and WT-mock groups (Figure S4C, P < .0001, ob/ob-SARS-CoV-2 vs ob/ob-mock group; P = .0211, WT-SARS-CoV-2 vs WT-mock group; n = 4 in WT-mock and WT-SARS-CoV-2 groups, n = 12 in ob/ob-mock and ob/ob-SARS-CoV-2 groups). Our data suggested that the preexisting underlying diseases aggravated pulmonary defects after SARS-CoV-2 infection.

We quantified viral RNA by real-time PCR using lung tissues. We found that the viral RNA copies were $10^{7.04}$, $10^{8.01}$, $10^{7.69}$, and $10^{7.13}$ copies/mL, respectively, in four SARS-CoV-2 groups (Figure 1E, n = 4 in WT-mock and WT-SARS-CoV-2 groups; n = 5 in ADR-mock group and n = 10 in ADR-SARS-CoV-2 group; n = 3 in cTnT^{R141W}-mock group and n = 5 in cTnT^{R141W}-SARS-CoV-2 group; n = 12 in ob/ob-mock and ob/ob-SARS-CoV-2 groups). However, no statistically significant of viral RNA loads between these four SARS-CoV-2 groups.

In addition, we performed immunofluorescence to detect the co-localization of SARS-Cov-2 S protein and hACE2 receptor in alveolar epithelial cells in lung tissues from SARS-CoV-2 and mock groups (Figure 1F, and Figure S5). Meanwhile, the virus infection was further confirmed by in situ hybridization (ISH) in lung tissues (Figure 1G,H).

In the WT-SARS-CoV-2 group, the damaged lungs became swollen and enlarged as compared to the WT-mock mice, which showed homogeneously pink and slightly deflated lung lobes, by gross and histopathologic analyses (Figure 1G). The WT-SARS-CoV-2 group also showed multifocal lesions with coalescent scattered-dark reddish-purple areas and focal palpable nodules throughout the lung lobes. Microscopically, the lung tissues from WT-SARS-CoV-2 mice displayed moderate interstitial pneumonia, which was characterized by the infiltration and accumulation of inflammatory cells and thickened alveolar septa throughout the right robe of the lung. In addition, perivasculitis and peribronchitis were observed in the lung of WT-SARS-CoV-2 group (Figure 1G,I,J). Compared with WT-SARS-CoV-2 mice, damaged lungs in CVD and DM mice became more swollen and enlarged, with multifocal scattered-dark reddish-purple areas throughout the lung
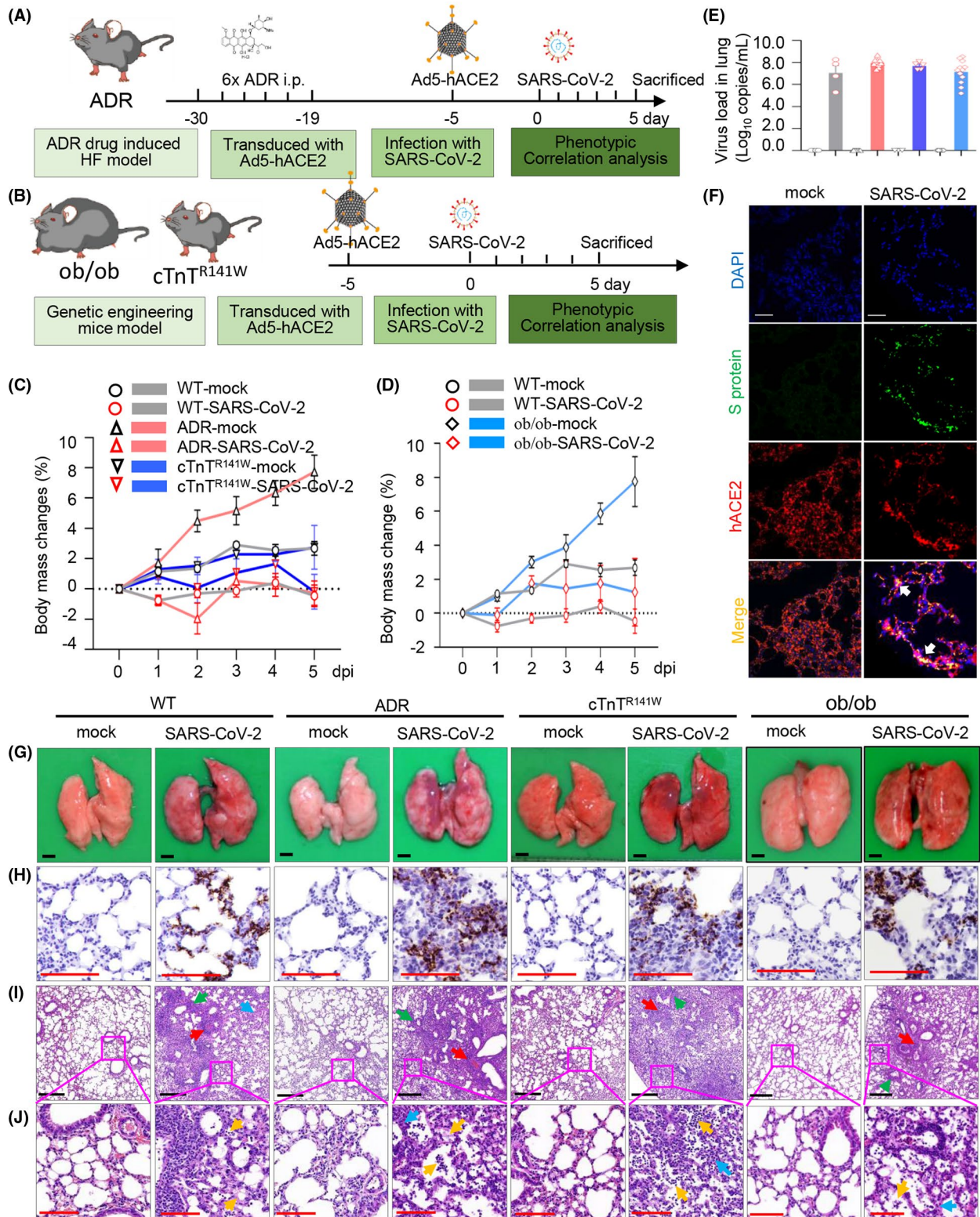
FIGURE 1 Preexisting CVDs and DM exacerbates the histopathologic changes in pneumonia during SARS-CoV-2 infection. Schematic diagram of study strategy on ADR-induced myocardial injury comorbid mice model (A), cTnT^{R141W} familial dilated cardiomyopathy (FDCM) comorbid mice model, and ob/ob diabetic comorbid mice model (B). Weight changes (C and D) were monitored daily after received SARS-CoV-2, and virus load (E) at 5 d post–SARS-CoV-2 or mock intranasally (n = 4 in WT-mock and WT-SARS-CoV-2 groups, n = 5 in ADR-mock and n = 10 in ADR-SARS-CoV-2 groups, n = 3 in cTnT^{R141W}-mock and n = 5 in cTnT^{R141W}-SARS-CoV-2 groups; n = 12 in ob/ob-mock and ob/ob -SARS-CoV-2 groups). The co-localization of SARS-CoV-2 S protein and hACE2 receptor (F) was detected by immunofluorescence (anti-SARS-CoV-2 S protein antibody (green), anti-human ACE2 antibody (red) and DAPI (blue), n = 3 per group, white bar = 100 μm). Viral RNA was detected using ISH in lung tissues (G-H). Postmortem examination showed multifocally scattered-dark reddish purple areas and palpable nodules from lung at 5dpi (G), and histopathologic observation indicated that moderate interstitial pneumonia with infiltration of lymphocytes (yellow arrow) and thickened alveolar septa (blue arrow), and serious perivasculitis (red arrow) and peribronchitis (green arrow) were also shown in SARS-CoV-2 groups (I-J, n = 3 per group, black bar = 400 μm, red bar = 100 μm)

---

lobes. Microscopically, comorbid mice displayed more severe pneumonia phenotypes, including infiltration of inflammatory cells, thickened alveolar septa, and perivasculitis (Figure 1,J).

3.3 | Comorbid mice showed impaired inflammatory factors production during SARS-CoV-2 infection

Inflammatory factors were involved in immune response and viral RNA clearance during SARS-CoV-2 infection. Then we tested the expression levels of inflammatory factors, IL-6, TNF-α, IFN-γ, and IL-10, in mice lung. Our data showed that pro-inflammatory factors, including IL-6, TNF-α, IFN-γ, and anti-inflammatory factor IL-10 were significantly increased after SARS-CoV-2 infection (Figure 2A-F, n = 4 in WT-mock and WT-SARS-CoV-2 group, n = 5 in ADR-mock and ADR-SARS-CoV-2 group, n = 3 in cTnT^{R141W}-mock and n = 5 in cTnT^{R141W}-SARS-CoV-2 group, n = 5 in ob/ob-mock and ob/ob-SARS-CoV-2 group). We also detected the inflammatory factors production cells aggregation, such as macrophage cells (Figure 2G). Recent study indicated that the IFN production contributed to viral RNA clearance and related to the severity of COVID-19 in patients.[18,19] In our comorbid mouse models, the production of pro-inflammatory factors IL-6, TNF-α, and IFN-γ was impaired in CVD and DM models with SARS-CoV-2 infection. This may indicate that the impairment of immune response and reduction of viral RNA clearance result in bad histopathologic changes in comorbid mouse models. The impairment of anti-inflammatory factor IL-10 production was also observed in DM model, but not in CVD models (Figure 2B,E). Furthermore, we tested the IFN-related innate immune response pathway. Our western blot results suggested impairment of JAK/STAT innate immune responses in comorbid mouse models (Figure 2H-O). Impairment of innate immune response and decreased IFN-γ production may indicate the severity of pneumonia and histopathologic changes in underlying disease mice model with SARS-CoV-2 infection.

3.4 | SARS-CoV-2 infection aggravated myocardial injury in cardiovascular comorbid mice

We then examined the impact of SARS-CoV-2 infection on the heart of CVD comorbidities. The heart weight in the WT-SARS-CoV-2 and cTnT^{R141W}-SARS-CoV-2 groups was slightly higher than that of their respective mock groups, but given no significance, and SARS-CoV-2 infection resulted in decrease in heart weight in the ADR-SARS-CoV-2 group (Figure 3A, P = .0122, ADR-SARS-CoV-2 vs ADR-mock group; P = .5317, cTnT^{R141W}-SARS-CoV-2 vs cTnT^{R141W}-mock group; n = 4 in WT-mock and WT-SARS-CoV-2 group; n = 5 in ADR-mock group, n = 10 in ADR-SARS-CoV-2 group; n = 3 in cTnT^{R141W}-mock group, n = 5 in cTnT^{R141W}-SARS-CoV-2 group).

Strikingly, viral RNA can be detected in the myocardium of CVD models on SARS-CoV-2 infection, at about $10^{4.27}$ copies/mL (Figures 3B, 2/10, 20% in ADR-SARS-CoV-2 group) and $10^{4.12}$ copies/mL (Figures 3B, 2/5, 40.0% in cTnT^{R141W}-SARS-CoV-2 group), while no viral RNA could be detected in WT-SARS-CoV-2 mice. Thus, preexisting cardiovascular diseases increased the risk of SARS-CoV-2 infection in myocardium. Furthermore, we found that SARS-CoV-2 S protein could be detected in the myocardium in our CVD mice after SARS-CoV-2 infection (Figure 3C).

Acute myocardial injury markers such as NT-proBNP and cTnI were determined. We found that NT-proBNP significantly increased in peripheral blood in the WT-SARS-CoV-2 group than in the WT-mock group, as determined using ELISA, while NT-proBNP level increased in both the CVD comorbid groups than in their respective mock groups (Figure 3D, P = .0375, WT-SARS-CoV-2 vs WT-mock group; P < .0001, ADR-SARS-CoV-2 vs ADR-mock group; P = .0035, cTnT^{R141W}-SARS-CoV-2 vs cTnT^{R141W}-mock group; n = 4 in WT-mock and WT-SARS-CoV-2 group; n = 5 in ADR-mock group, n = 10 in ADR-SARS-CoV-2 group; n = 3 in cTnT^{R141W}-mock group, n = 5 in cTnT^{R141W}-SARS-CoV-2 group). It also showed that cTnI level increased significantly in the myocardium in both CVD mice than in the WT mice with SARS-CoV-2 infection, as measured using western blot (Figure 3E-G, P = 0.0E-G, P = 081, WT-SARS-CoV-2 vs WT-mock group; P = .0003, ADR-SARS-CoV-2 vs ADR-mock group; P < .0001, cTnT^{R141W}-SARS-CoV-2 vs cTnT^{R141W}-mock group; n = 4 per group).

Cardiomyocyte hypertrophy and myofibril disarray were observed in WT-SARS-CoV-2 mice, and these phenotypes appeared more severe in CVD comorbid mice. ADR-SARS-CoV-2 mice exhibited thin wall, reduced heart weight, myocardial damage, and increased cardiac fibrosis, while cTnT^{R141W}-SARS-CoV-2 mice exhibited thin wall, larger chamber, heavier heart weight, myocyte malalignment, and increased collagen deposition as demonstrated using H&E
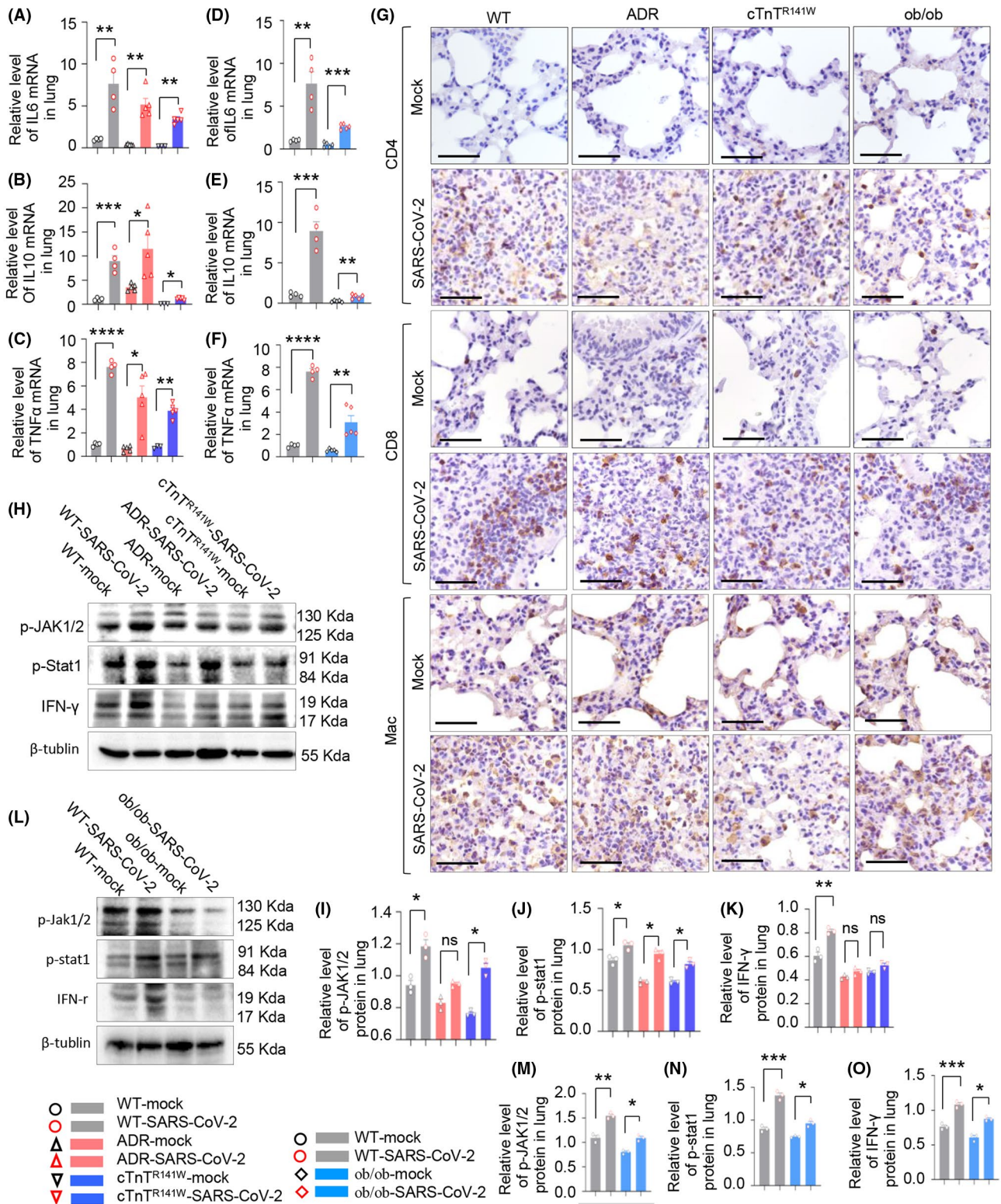
FIGURE 2 Comorbid mice showed impaired innate immune responses during SARS-CoV-2 infection. A-F, The mRNA level of IL-6, IL-10, and TNF-α in WT-mock, WT-SARS-CoV-2, ADR-mock, ADR-SARS-CoV-2, cTnT^{R141W}-mock, and cTnT^{R141W}-SARS-CoV-2 groups or in WT-mock, WT-SARS-CoV-2, ob/ob-mock, and ob/ob-SARS-CoV-2 groups. G, Immunohistochemistry analysis of CD4, CD8, and Mac cells in all the comorbid mice models. H-O, Protein expression of p-JAK1/2, p-Stat1 and IFN-γ were detected in six CVD comorbid groups and four DM comorbid groups by western blot. *$P < .05$, **$P < .01$, ***$P < .001$ and ****$P < .001$ vs respective mock groups, n = 3 per group
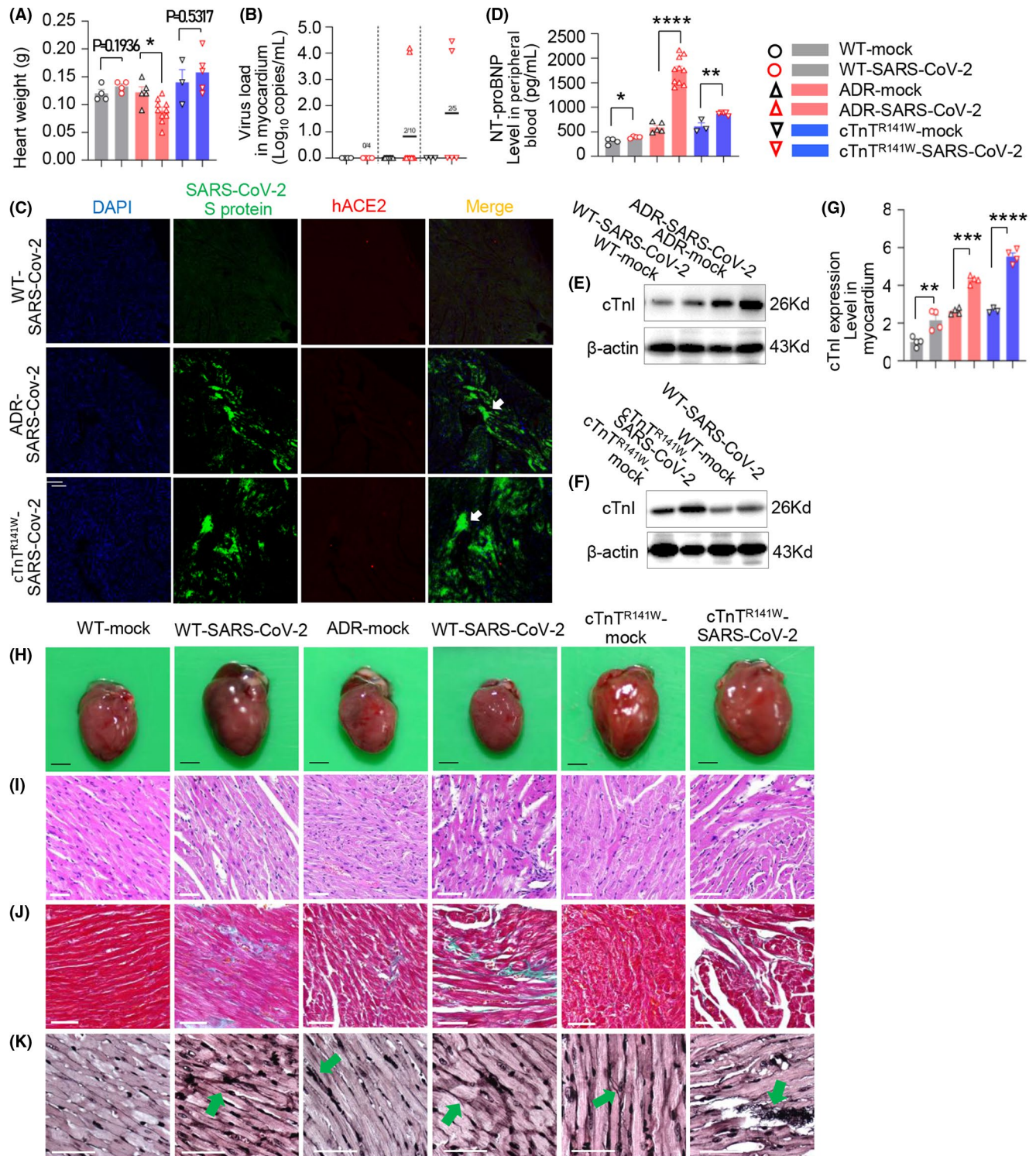
FIGURE 3 SARS-CoV-2 infection aggravated myocardial injury in cardiovascular comorbid mice. A, Heart weight at 5 dpi (*$P < .05$ vs ADR-mock group). B, Viral RNA detected by real-time PCR, about $10^{4.27}$ copies/mL, in myocardium of 2/10 (20%) mice from ADR-SARS-CoV-2 group, about $10^{4.12}$ copies/mL, in myocardium of 2/5 (40%) mice from cTnT^{R141W}-SARS-CoV-2 group at 5 dpi (n = 5 in ADR-mock and n = 10 in ADR-SARS-CoV-2 groups, n = 3 in cTnT^{R141W}-mock and n = 5 in cTnT^{R141W}-SARS-CoV-2 groups). C, The localization of SARS-CoV-2 S protein and hACE2 receptor detected by immunofluorescence in heart tissues, and the sections were incubated with anti-SARS-CoV-2 S protein antibody (green), anti-human ACE2 antibody (red), and DAPI (blue). SARS-CoV-2 S protein was demonstrated in myocardium in SARS-CoV-2 group (white arrow, n = 3 per group, white bar = 100 μm). D, NT-proBNP was detected in peripheral blood by Elisa at 5dpi (n = 4 in WT-mock and WT-SARS-CoV-2 groups, n = 5 in ADR-mock and n = 10 in ADR-SARS-CoV-2 groups, n = 3 in cTnT^{R141W}-mock and n = 5 in cTnT^{R141W}-SARS-CoV-2 groups). E-G, cTnI was detected by western blot (n = 4 per group) in myocardium at 5 dpi (*$P < .05$, **$P < .01$, ****$P < .0001$ vs respective mock group). H&E staining of the whole-heart transverse sections (H, black bar = 2 mm), and magnification of H&E (I), Masson trichrome-stained (J) and silver staining (K) in myocardium section at 5 dpi (white bar = 50 μm)

staining and mason trichrome staining (Figure 3H-J). Furthermore, it exhibited more severe nerve fibers break and entangle in CVD comorbid mice by argentation (Figure 3K).

3.5 | Mitochondrial injury and oxidative stress and apoptosis of cardiomyocytes contribute to myocardial injury in CVD comorbid mice

Next, we analyze the possible mechanisms that cause myocardial damage. Inflammatory activation and cytokine release could lead to oxidative stress, and we found that SOD1, SOD2, and iNOS increased more in our two CVD comorbid mice groups than in the WT group when compared with respective mock groups (Figure 4C, n = 3 per group), which indicated the accumulation of oxidative stress products. Meanwhile, we found that GPX1 and GST levels decreased in our CVD comorbid mice group than in the WT mice group when compared with their respective mock groups (Figure 4D,E, n = 3 per group), which indicated that the decrease in the scavenging ability of oxidative stress products.

Then, we found that disrupted ultrastructure, including swollen mitochondria with loss of cristae and vacuolization, poorly organized myofibrils with diffusion, damage, and lysis were more severe in CVD comorbid mice after SARS-CoV-2 infection as observed using transmission electron microscopy (TEM) (Figure 4F). We then detected the expression of marker proteins of mitochondrial complex I, II and III, and key enzyme in tricarboxylic acid cycle using western blot. We also found that NDUFS3 (core subunit of complex I), NUBPL (core subunit of complex I), SDHB (involved in electron transport in the complex II), UQCRC2 (core subunit of complex III), and ACO2 (aconitase 2, participates in ATP generation) decreased significantly in our two CVD comorbid mice groups than in the WT group when compared with respective mock groups (Figure 4G-L, n = 3 per group).

The structure and function of mitochondria are obviously damaged, which could further lead to a caspase cascade. We found that Fas was increased significantly and caspases 8, 9, and 3 were activated in our two CVD comorbid mice group than in the WT group when compared with their respective mock groups (Figure 4G,M-P, n = 3 per group).

Our result suggested that oxidative stress induced by the inflammatory response further damaged the structure and function of mitochondria. Therefore, the mitochondria-dependent apoptotic pathway was activated and induced myocardial apoptosis, which together with the abnormally increased inflammatory response in myocardium led to myocardial injury (Figure 4O).

3.6 | SARS-CoV-2 infection aggravated blood glucose control and bone metabolism in diabetes mice

During SARS-CoV-2 infection, we found that fast blood glucose increased in the WT-SARS-CoV-2 group when compared with the WT-mock group, but given no significance, and this index increased remarkably in our comorbid diabetic mice (Figure 5A, P = .0728, WT-SARS-CoV-2 vs WT-mock group; P = .0198, ob/ob-SARS-CoV-2 vs ob/ob-mock group; n = 4 in WT-mock and WT-SARS-CoV-2 group, n = 6 in ob/ob-mock and ob/ob-SARS-CoV-2 group). We also observed decreased insulin tolerance test (ITT) response (Figure 5B-C).

As we know, the biochemical parameters, such as triglyceride (TG), low-density lipoprotein (LDL), high-density lipoprotein (HDL), and total cholesterol (TC) are significantly higher in ob/ob mice than in WT mice.[20] Here, we performed the biochemical analysis during SARS-CoV-2 infection. Our data showed decreased in TG (Figure 5D, P = .57742, WT-SARS-CoV-2 vs WT-mock group; P = .0053, ob/ob-SARS-CoV-2 vs ob/ob-mock group; n = 4 in WT-mock and WT-SARS-CoV-2 group, n = 6 in ob/ob-mock and ob/ob-SARS-CoV-2 group), but no significant changes in LDL, ALP, γ-GT, HDL, ApoA1, AST/ALT, and TC in our comorbid diabetic model (Figure S6A-G).

Bone volume and BMD also decreased in ob/ob mice. In order to determine whether SARS-CoV-2 infection affects bone development in ob/ob mice, we performed the microcomputed tomography (micro-CT) and microarchitecture measurements of femurs in mice. Micro-CT imaging results showed remarkable differences in trabecular bone volume between the ob/ob-mock group and ob/ob-SARS-CoV-2 group (Figure 5E). Our results showed volumetric BMD (Figure 5F, P = .3752, WT-SARS-CoV-2 vs WT-mock group; P = .0232, ob/ob-SARS-CoV-2 vs ob/ob-mock group; n = 3 per group), trabecular bone volume (BV/TV, Figure 5G, P = .7982, WT-SARS-CoV-2 vs WT-mock group; P = .0242, ob/ob-SARS-CoV-2 vs ob/ob-mock group), and trabecular number (Tb.N, Figure 5H, P = .8864, WT-SARS-CoV-2 vs WT-mock group; P = .0417, ob/ob-SARS-CoV-2 vs ob/ob-mock group) decreased significantly. The trabecular thickness (Tb.Th, Figure 5I, P = .9419, WT-SARS-CoV-2 vs WT-mock group; P = .0867, ob/ob-SARS-CoV-2 vs ob/ob-mock group) also decreased but there is no significance. The trabecular separation (Tb. Sp, Figure 5J, P = .8512, WT-SARS-CoV-2 vs WT-mock group; P = .0088, ob/ob-SARS-CoV-2 vs ob/ob-mock group) increased significantly. Our results showed that SARS-CoV-2 infection perturbed bone metabolism and development in diabetic mice. WNT signal is critical for bone development; our western blot result showed no significant difference in GSK-3β and β-catenin between the SARS-CoV2 group and mock group (data not shown). Our data showed PI3K/AKT/mToR signal was impaired during SARS-CoV-2 infection (Figure 5K-N). This impairment may related to the bone loss during SARS-CoV-2 infection in DM model (Figure 5O).

4 | DISCUSSION

Patients with chronic diseases, such as CVDs and DM, exhibited increased risks in viral infection-related diseases.[21] CVDs and DM are the top two comorbidities that increase the severity and mortality of the COVID-19.[1-4] Therefore, it is an urgent need to understand
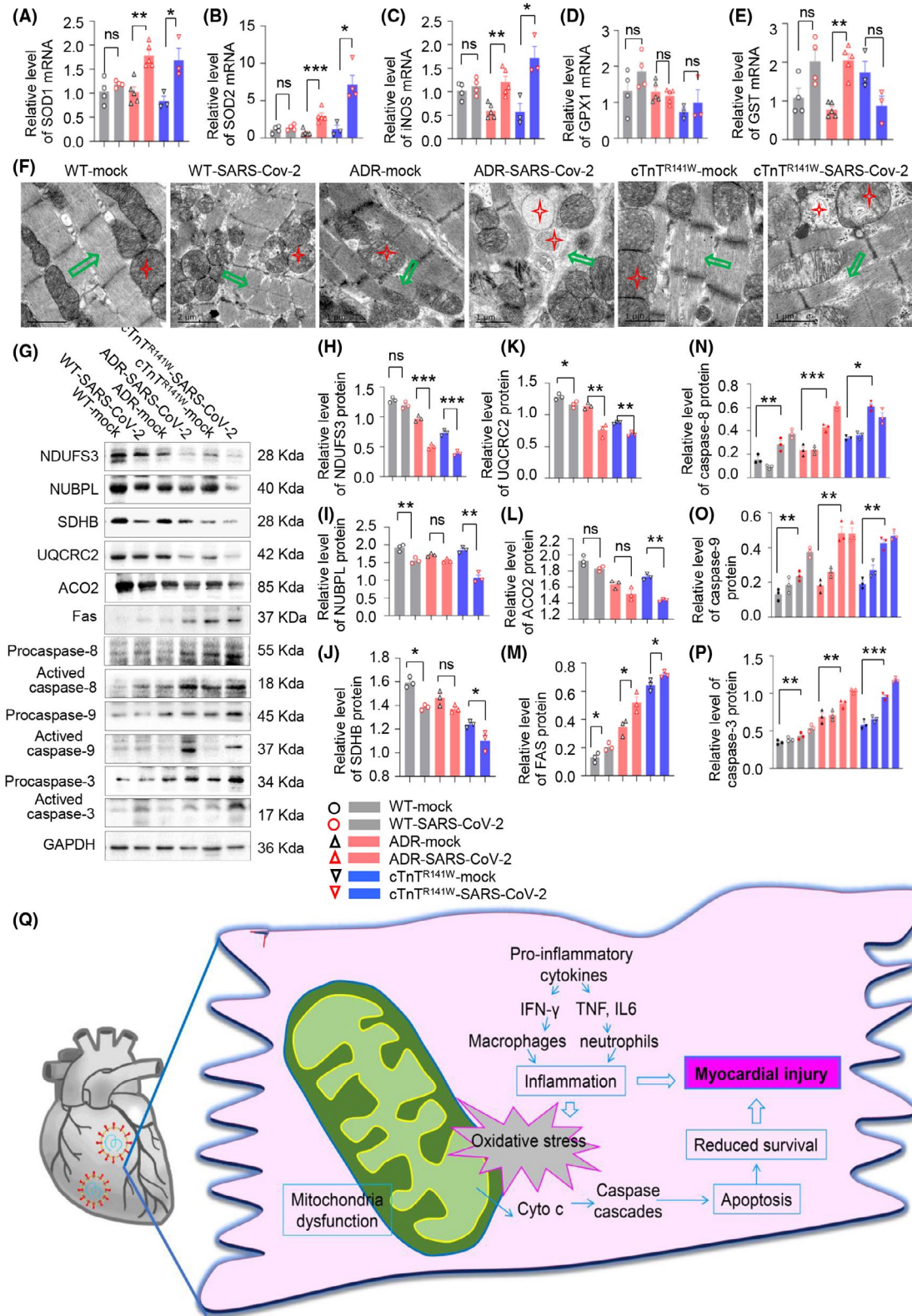
FIGURE 4 Mitochondrial injury and oxidative stress and apoptosis of cardiomyocytes contribute to myocardial injury in CVD comorbid mice. A-E, The mRNA level of SOD1, SOD2, iNOS, GPX1, and GST in WT-mock, WT-SARS-CoV-2, ADR-mock, ADR-SARS-CoV-2, cTnT^{R141W}-mock, and cTnT^{R141W}-SARS-CoV-2 groups. (F) Damaged mitochondria were observed through transmission electron microscopy (TEM) in myocardium from six groups (red star indicated mitochondria and green arrow indicated myocardial fibrosis). Protein expression of NDUFS3, NUBPL, SDHB, UQCRC2, ACO2, pro-caspase-8, activated caspase-8, pro-caspase-9, activated caspase-9, pro-caspase-3, and activated caspase-3 were detected by western blot (G-P). *$P < .05$, **$P < .01$, ***$P < .001$ vs respective mock groups, n = 3 per group. Schematic diagram for pathogenic mechanism of myocardial damage in CVD comorbid mice (Q)
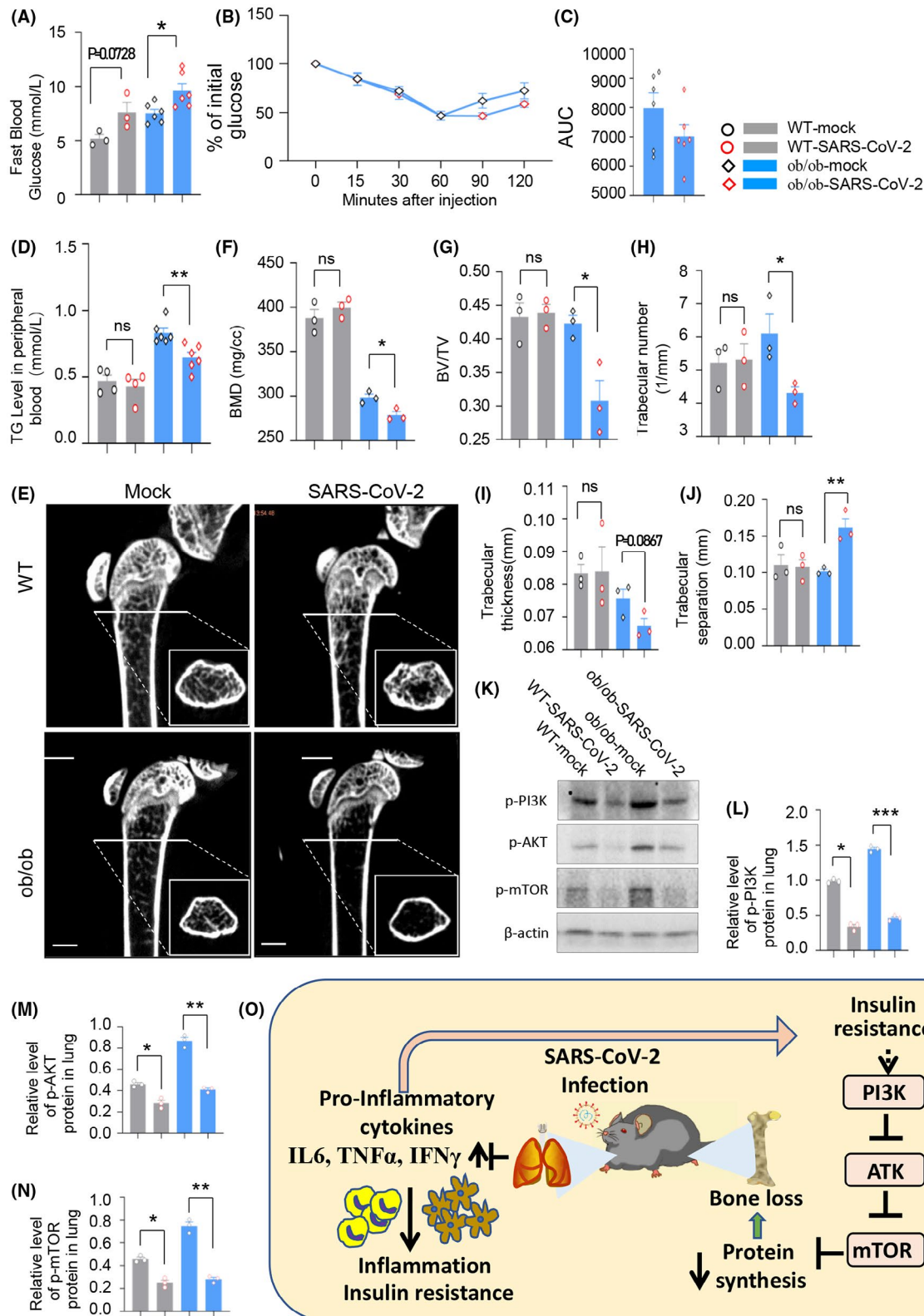
FIGURE 5 SARS-CoV-2 infection aggravated blood glucose control and bone metabolism in diabetes diseases mice. A, Fast blood glucose at 5 dpi (*P < .05 vs ob/ob-mock group, n = 4 in WT-mock and WT-SARS-CoV-2 groups, n = 6 in ob/ob-mock and ob/ob -SARS-CoV-2 groups). B and C, Insulin tolerance test was performed. SARS-CoV-2–infected ob/ob mice showed decreased glucose regulation response. D, Triglyceride (TG) at 5 dpi performed by biochemical analysis (**P < .01 vs ob/ob-mock group; n = 4 in WT-mock and WT-SARS-CoV-2 groups, n = 6 in ob/ob-mock and ob/ob -SARS-CoV-2 groups). E, Screenshot of microcomputed tomography (micro-CT) measurements of femurs in mice. F-J, Bone mineral density (BMD), trabecular bone volume (BV/TV), trabecular number (Tb.N), trabecular thickness (Tb.Th), and trabecular separation (Tb.Sp) at 5 dpi (n = 3 per group, *P < .05, **P < .01 vs ob/ob-mock group). Protein expression of p-PI3K, p-AKT, and p-mTOR were detected by western blot (K-N). Schematic diagram of pathogenic mechanism of target organ in DM comorbid mice (O)

the pathogenesis mechanism of comorbidity associated with chronic diseases.

In this study, we generated a versatile and powerful tool to produce comorbid animal models to mimic the clinical phenotypes of SARS-CoV-2–infected patients with preexisting diseases. The replication-deficient adenovirus-mediated gene delivery to murine lungs has been applied to SARS-CoV, MERS, and SARS-CoV-2 related study.[10,11] This strategy provides a valuable tool to understand the interplay of underlying comorbidities and COVID-19. To optimize the ectopic expression of hACE2 in murine lungs, here we tested several different virus strategies including lentivirus, replication-deficient adenovirus (Ad5), and adeno-associated virus (AAV). Among them, adenovirus mediated the highest hACE2 expression level. Here, we applied these viral vectors to other disease mouse models to produce CVD and DM comorbid mice models. We observed more severe pathological phenotypes of pneumonia and serious histopathologic changes in the lung in the comorbid models after SARS-CoV-2 infection when compared to control mice. This provides a tool to study the interplay of preexisting diseases and SARS-CoV-2 infection.

Our CVD and DM comorbid mouse models exhibited impaired innate immune responses, because increased inflammatory factors such as as IL-6, IL-10, and TNF-α, aggregated inflammatory factors production cells such as CD4+ T cells, CD8+ T cells, and macrophage, impaired Jak/Stat/IFN-γ immunoprotective pathway. Those observations may partly explain why comorbid mice showed aggravating pneumonia phenotypes. At the same time, we further analyzed the manifestation of the target organs and the possible pathogenic mechanisms in CVD and DM comorbid mice models in this study.

Here the widely used cardiomyopathy model and/or HF induced by ADR, and heart-specific cTnT^{R141W} overexpression transgenic mice with typical DCM phenotypes were previously established and reported in our laboratory.[15,22,23] These two CVD comorbid mouse models exhibited similar phenotypes and could mimicked the complex pathological symptoms of COVID-19 patients with preexisting cardiovascular, including interstitial pneumonia, elevated markers of myocardial injury, including NT-proBNP and cTnI, myocardial histological changes, including disordered arrangement and rupture of the myocardium. Furthermore, preexisting CVDs increased the risk of SARS-CoV-2 infection in myocardium, and SARS-CoV-2 infection aggravated myocardial defects in our comorbid models.

It is reported that hospitalized patients develop acute COVID-19 cardiovascular syndrome (ACovCS), which is mostly presented as an acute cardiac injury. Myocardial injury is common among patients with COVID-19 infection and highly correlates with disease severity and in-hospital mortality.[24–27] Till now, there are several speculations on the specific mechanism of myocardial injury induced by SARS-CoV-2 infection. Cardiac involvement in COVID-19 seems to be a result of an inflammatory storm in response to the infection. Moreover, direct viral invasion of cardiomyocytes, as well as a myocardial injury due to oxidative stress, may account for acute cardiac injury in COVID-19. Nevertheless, the mechanism of heart injury

in COVID-19 is not clear yet.[21,28–30] It is reported that acute viral infection produces pro-inflammatory cytokine level elevations, and infiltrating macrophage is a source of superoxide, and inflammation resulting in increased oxidative stress and evolvement of apoptotic cardiomyocytes, finally contributing to myocardial injury.

Taken together, our studies showed that the myocardial oxidative stress level increased significantly after SARS-CoV-2 infection, the mitochondrial structure and function were impaired, and the mitochondria-dependent apoptotic pathway was activated and induce myocardial apoptosis, which together with the abnormal increased inflammatory response in myocardium, jointly led to myocardial injury.

Several reports have shown that diabetes was also highly relevant with severe illness and death in COVID-19.[31] Among 1099 COVID-19 patients in China, diabetes was present in 26.9% of patients achieving severity, or death, compared with 6.1% if none of primary disease. In another report from American CDC, among 7162 COVID-19 patients, diabetes was present in 24% of non-ICU and 32% of ICU patients.[32] In our diabetic comorbid model, SARS-CoV-2 infection caused more severe histopathologic phenotypes as compared to WT-SARS-CoV-2 group or their respective mock group. This suggests that the presence of hyperglycemia is associated with the adverse outcome of SARS-CoV-2 infection. Moreover, SARS-CoV-2 infection increased the blood glucose level both in diabetes model and WT group. This was consistent with the fact that SARS-CoV-2–infected patients exhibit increased blood glucose.[33]

Previous report showed that abnormal blood glucose might impair the immune response to the viral infection and lead to secondary damages to the lungs.[34] Here, we detected that the fasting blood glucose increased both in WT-SARS-CoV-2 and ob/ob-SARS-CoV-2. The changes were more dramatic in our diabetic comorbid mice models than in WT mice. In addition, we also observed a significant increase of inflammatory cytokines, including IL-6, IL-10, TNF-α, and IFN-γ in the lung tissues, which was often referred to as a cytokine storm. This may further aggravate the adverse outcome during infection. We also observed reduced ITT response and this may suggest SARS-CoV-2 infection further impaired the blood glucose regulation. Maybe due to the short infection period, further damage to β-cell was not observed in both the WT-SARS-CoV-2 group and ob/ob-SARS-CoV-2 groups when compared with their mock groups (data not shown). Surprisingly, even in a short SARS-CoV-2 infection period, we detected significant decrease in bone mineral density (BMD) and this was not reported in patients yet. Our results suggest that patients with osteoporosis are likely at a high risk of adverse outcome from SARS-CoV-2 infection and need more intensive care. Our data suggested that PI3K/AKT/mTOR pathway, but not WNT signal pathway, was involved in the DM model bone loss during SARS-CoV-2 infection.

In summary, we established a versatile strategy to build comorbid models, and our comorbid mouse models mimicked the complex pathological symptoms of COVID-19 patients with preexisting cardiovascular or diabetic diseases. They both showed impairments of immune response during SARS-CoV-2 infection, which result in damage in their related target organs. Our study provides clues to

understand the characteristics of the interaction between the underlying disease and SARS-CoV-2 virus as well as possible intervention targets and directions.

CONFLICT OF INTEREST

The authors declare no competing interests.

AUTHOR CONTRIBUTIONS

C. Q., L. Z., Y. M., and D. L designed the experiments. Y. M., D. L., X. Q., L. B., Y. Q., J. L., XQ, LY, X. Z., FQ, YL, XS, CS, JL, JW, YH, KG, WD, NL, SG, JX, QW, SP, and HG performed the experiments. Y. M., D. L., and X Q., collected and analyzed the data, and wrote the manuscript.

ORCID

Yuanwu Ma (iD) https://orcid.org/0000-0002-1882-1777
Qi Lv (iD) https://orcid.org/0000-0003-2102-2877
Jing Xue (iD) https://orcid.org/0000-0002-9113-2433
Lianfeng Zhang (iD) https://orcid.org/0000-0002-5774-2924
Chuan Qin (iD) https://orcid.org/0000-0002-6261-1232

REFERENCES

1. Bonow RO, Fonarow GC, O'Gara PT, Yancy CW. Association of coronavirus disease 2019 (COVID-19) with myocardial injury and mortality. *JAMA Cardiol*. 2020;5:751-753.
2. Epidemiology Working Group for Ncip Epidemic Response, C.C.f.D.C., and Prevention. The epidemiological characteristics of an outbreak of 2019 novel coronavirus diseases (COVID-19) in China. *Zhonghua Liu Xing Bing Xue Za Zhi*. 2020;41:145-151.
3. Ruan S. Likelihood of survival of coronavirus disease 2019. *Lancet Infect Dis*. 2020;20:630-631.
4. Team, T.N.C.P.E.R.E. The epidemiological characteristics of an outbreak of 2019 novel coronavirus diseases (COVID-19)-China. *China CDC Weekly*. 2020b;2:113-122.
5. Banik GR, Alqahtani AS, Booy R, Rashid H. Risk factors for severity and mortality in patients with MERS-CoV: analysis of publicly available data from Saudi Arabia. *Virol Sin*. 2016;31:81-84.
6. Zhou P, Yang XL, Wang XG, et al. A pneumonia outbreak associated with a new coronavirus of probable bat origin. *Nature*. 2020;579:270-273.
7. Bao L, Deng W, Huang B, et al. The pathogenicity of SARS-CoV-2 in hACE2 transgenic mice. *Nature*. 2020;583:830-833.
8. Jiang RD, Liu MQ, Chen Y, et al. Pathogenesis of SARS-CoV-2 in transgenic mice expressing human angiotensin-converting enzyme 2. *Cell*. 2020;182(50-58):e58.
9. Sun SH, Chen Q, Gu HJ, et al. A mouse model of SARS-CoV-2 infection and pathogenesis. *Cell Host Microbe*. 2020c;28(124-133):e124.
10. Hassan AO, Case JB, Winkler ES, et al. A SARS-CoV-2 infection model in mice demonstrates protection by neutralizing antibodies. *Cell*. 2020;182:744-753.e4.
11. Sun J, Zhuang Z, Zheng J, et al. Generation of a broadly useful model for COVID-19 pathogenesis, vaccination, and treatment. *Cell*. 2020;182:734-743.
12. Guan F, Yang X, Li J, et al. New molecular mechanism underlying Myc-mediated cytochrome P450 2E1 upregulation in apoptosis and energy metabolism in the myocardium. *J Am Heart Assoc*. 2019;8:e009871.
13. Lu D, Ma Y, Zhang W, et al. Knockdown of cytochrome P450 2E1 inhibits oxidative stress and apoptosis in the cTnTR141W dilated cardiomyopathy transgenic mice. *Hypertension*. 2012b;60:81-89.
14. Lu D, Zhang L, Bao D, et al. Calponin1 inhibits dilated cardiomyopathy development in mice through the εPKC pathway. *Int J Cardiol*. 2014b;173:146-153.
15. Lu D, Bao D, Dong W, et al. Dkk3 prevents familial dilated cardiomyopathy development through Wnt pathway. *Lab Invest*. 2016;96:239-248.
16. Lu D, Dong W, Zhang X, et al. WIF1 causes dysfunction of heart in transgenic mice. *Transgenic Res*. 2013;22:1179-1189.
17. Lu D, Wang J, Li J, et al. Meox1 accelerates myocardial hypertrophic decompensation through Gata4. *Cardiovasc Res*. 2018;114:300-311.
18. Bastard P, Rosen LB, Zhang Q, et al. Autoantibodies against type I IFNs in patients with life-threatening COVID-19. *Science*. 2020;370:eabd4585.
19. Zhang Q, Bastard P, Liu Z, et al. Inborn errors of type I IFN immunity in patients with life-threatening COVID-19. *Science*. 2020;370:eabd4570.
20. Westman S. Development of the obese-hyperglycaemic syndrome in mice. *Diabetologia*. 1968;4:141-149.
21. Guzik TJ, Mohiddin SA, Dimarco A, et al. COVID-19 and the cardiovascular system: implications for risk assessment, diagnosis, and treatment options. *Cardiovasc Res*. 2020;116:1666-1687.
22. Lu D, Ma Y, Zhang W, et al. Knockdown of cytochrome P450 2E1 inhibits oxidative stress and apoptosis in the cTnT(R141W) dilated cardiomyopathy transgenic mice. *Hypertension*. 2012a;60:81-89.
23. Lu D, Zhang L, Bao D, et al. Calponin1 inhibits dilated cardiomyopathy development in mice through the epsilonPKC pathway. *Int J Cardiol*. 2014a;173:146-153.
24. Chen C, Chen C, Yan JT, Zhou N, Zhao JP, Wang DW. Analysis of myocardial injury in patients with COVID-19 and association between concomitant cardiovascular diseases and severity of COVID-19. *Zhonghua Xin Xue Guan Bing Za Zhi*. 2020a;48:567-571.
25. Guo T, Fan Y, Chen M, et al. Cardiovascular implications of fatal outcomes of patients with coronavirus disease 2019 (COVID-19). *JAMA Cardiol*. 2020;5:811-818.
26. He XW, Lai JS, Cheng J, et al. Impact of complicated myocardial injury on the clinical outcome of severe or critically ill COVID-19 patients. *Zhonghua Xin Xue Guan Bing Za Zhi*. 2020;48:456-460.
27. Magadum A, Kishore R. Cardiovascular manifestations of COVID-19 infection. *Cells*. 2020;19(9):2508.
28. Chen L, Li X, Chen M, Feng Y, Xiong C. The ACE2 expression in human heart indicates new potential mechanism of heart injury among patients infected with SARS-CoV-2. *Cardiovasc Res*. 2020b;116:1097-1100.
29. Hendren NS, Drazner MH, Bozkurt B, Cooper LT Jr. Description and proposed management of the acute COVID-19 cardiovascular syndrome. *Circulation*. 2020;141:1903-1914.
30. Liu PP, Blet A, Smyth D, Li H. The Science underlying COVID-19: implications for the cardiovascular system. *Circulation*. 2020;142:68-78.
31. Guan WJ, Ni ZY, Hu Y, et al. Clinical characteristics of coronavirus disease 2019 in China. *N Engl J Med*. 2020;382:1708-1720.
32. Team, C.C.-R. Preliminary estimates of the prevalence of selected underlying health conditions among patients with coronavirus

disease 2019 - United States, February 12-March 28, 2020. *MMWR Morb Mortal Wkly Rep.* 2020a;69:382-386.

33. Mazucanti CH, Egan JM. SARS-CoV-2 disease severity and diabetes: why the connection and what is to be done? *Immunity Ageing.* 2020;17:21.

34. Hollstein T, Schulte DM, Schulz J, et al. Autoantibody-negative insulin-dependent diabetes mellitus after SARS-CoV-2 infection: a case report. *Nat Metab.* 2020;2:1021-1024.

35. Wu R, Liu XM, Sun JG, et al. DJ-1 maintains energy and glucose homeostasis by regulating the function of brown adipose tissue. *Cell Discovery.* 2017;3:16054.

SUPPORTING INFORMATION

Additional supporting information may be found online in the Supporting Information section.